A Consistent AVHRR Visible Calibration Record Based on Multiple Methods Applicable for the NOAA Degrading Orbits. Part II: Validation

DAVID R. DOELLING

NASA Langley Research Center, Hampton, Virginia

RAJENDRA BHATT, BENJAMIN R. SCARINO, ARUN GOPALAN, AND CONOR O. HANEY

Science Systems and Applications, Inc., Hampton, Virginia

PATRICK MINNIS AND KRISTOPHER M. BEDKA

NASA Langley Research Center, Hampton, Virginia

(Manuscript received 8 February 2016, in final form 15 July 2016)

ABSTRACT

Consistent cross-sensor Advanced Very High Resolution Radiometer (AVHRR) calibration coefficients are determined using desert, polar ice, and deep convective cloud (DCC) invariant Earth targets. The greatest AVHRR calibration challenge is the slow orbit degradation of the host satellite, which precesses toward a terminator orbit. This issue is solved by characterizing the invariant targets with *NOAA-16* AVHRR observed radiances that have been referenced to the *Aqua* Moderate Resolution Imaging Spectrometer (MODIS) calibration using simultaneous nadir overpass (SNO) observations. Another benefit of the *NOAA-16* invariant target–modeled reflectance method is that, because of the similarities among the AVHRR spectral response functions, a smaller spectral band adjustment factor is required than when establishing calibrations relative to a non-AVHRR reference instrument. The sensor- and band-specific calibration uncertainties, with respect to the calibration reference, are, on average, 2% and 3% for channels 1 and 2, respectively. The uncertainties are smaller for sensors that are in afternoon orbits, have longer records, and spend less time in terminator conditions.

The multiple invariant targets referenced to *Aqua* MODIS (MITRAM) AVHRR calibration coefficients are evaluated for individual target consistency, compared against *Aqua* MODIS/AVHRR SNOs, and selected published calibration gains. The MITRAM and SNO relative calibration biases mostly agree to within 1% for channels 1 and 2, respectively. The individual invariant target and MITRAM sensor relative calibration biases are mostly consistent to within 1% and 2% for channels 1 and 2, respectively. The differences between the MITRAM and other published calibrations are mostly attributed to the reference instrument calibration differences.

1. Introduction

This article, as the second part of a two-part paper, outlines a multiple invariant target calibration approach designed to produce consistent cross-sensor Advanced Very High Resolution Radiometer (AVHRR) visible channel calibration coefficients using desert, polar ice, and deep convective cloud (DCC) invariant targets. The greatest challenge in calibrating the AVHRR record is the slowly degrading orbits common to the NOAA series of satellites. The orbits eventually track across the terminator. Therefore, the invariant targets need to be characterized over all observed solar zenith angles (SZAs). The *NOAA-16* AVHRR radiances are used for this task because the satellite gradually drifted from an early afternoon orbit into a terminator orbit. For simplicity, the individual NOAA satellites are indicated with the abbreviation, *Nx*, where *x* refers to the satellite number. Over its lifetime, the *N16* AVHRR provided measurements for nearly all possible SZAs over all invariant targets. The *N16* AVHRR radiances are first referenced to the well-calibrated *Aqua* platform Moderate Resolution Imaging Spectroradiometer (MODIS) Collection 6 (C6) calibration by way of simultaneous nadir overpass (SNO) comparisons. Furthermore, characterizing the invariant targets with *N16* AVHRR

Corresponding author address: David Doelling, NASA Langley Research Center, MS 420, Hampton, VA 23681-2199.
E-mail: david.r.doelling@nasa.gov

DOI: 10.1175/JTECH-D-16-0042.1

TABLE 1. Launch dates, and start and end dates during which the MITRAM and SNO AVHRR calibration coefficients are valid. The table also includes the time range of the DCC and PICS datasets. The four-digit year and the three-digit day of year define the dates. Bold text denotes satellites in afternoon orbits.

			MITRAM				SNO[a]				DCC				PICS			
Satellite	Launch		Start		End		Start		End		Start		End		Start		End	
TIROS-N	**1978**	**286**	**1978**	**305**	**1980**	**031**					**1978**	**305**	**1980**	**031**	**1978**	**305**	**1980**	**031**
N6	1979	178	1980	001	1981	244					1980	001	1981	244	1980	032	1981	244
N7	**1981**	**174**	**1981**	**214**	**1985**	**031**					**1981**	**214**	**1985**	**031**	**1981**	**214**	**1985**	**031**
N8	1983	087	1983	245	1985	305					1983	245	1985	305	1983	245	1985	305
N9	**1984**	**347**	**1985**	**032**	**1988**	**335**					**1985**	**060**	**1988**	**273**	**1985**	**032**	**1988**	**335**
N10	1986	260	1986	305	1991	274					1986	305	1991	212	1986	305	1991	274
N11	**1988**	**268**	**1988**	**305**	**1994**	**274**					**1988**	**305**	**1994**	**212**	**1988**	**305**	**1994**	**274**
N12	1991	134	1991	244	1998	243					1991	274	1996	212	1991	244	1998	243
N14	**1994**	**364**	**1995**	**001**	**2001**	**273**					**1995**	**032**	**2000**	**244**	**1995**	**001**	**2001**	**273**
N15	1998	133	1998	274	2013	212	2002	219	2012	232	1999	121	2013	212	1998	274	2013	212
N16	**2000**	**265**	**2001**	**001**	**2012**	**366**	**2002**	**184**	**2014**	**156**	**2001**	**001**	**2012**	**366**	**2001**	**001**	**2012**	**366**
N17	2002	175	2002	182	2010	274	2002	191	2012	241	2002	182	2010	274	2002	182	2010	243
N18	**2005**	**140**	**2005**	**182**	**2014**	**304**	**2006**	**101**	**2014**	**232**	**2005**	**182**	**2014**	**273**	**2005**	**182**	**2014**	**304**
MetOp-A	2006	292	2007	121	2014	365	2007	152	2014	259	2007	152	2014	365	2007	121	2014	365
N19	**2009**	**037**	**2009**	**091**	**2014**	**365**	**2009**	**152**	**2014**	**248**	**2009**	**091**	**2014**	**365**	**2009**	**091**	**2014**	**365**
MetOp-B	2012	261	2013	001	2014	304	2013	153	2014	243	2013	032	2014	304	2013	001	2014	273

[a] SNOs include only the months of April–September.

radiances reduces spectral difference–induced uncertainties given that the spectral response functions (SRFs) of nearly all AVHRR sensors (excepting that on TIROS-N) are similar. Multiple invariant targets are used to reduce the impact of the natural variability associated with a single invariant target. The calibration consistency between the individual invariant targets and the *Aqua* MODIS SNO methods validates the approach.

Part I of this two-part article describes the desert, polar ice, DCC, and SNO calibration methods (Bhatt et al. 2016, hereafter Part I). Directional models (DM) are used to characterize the invariant targets by regressing the *N16* AVHRR observed TOA radiances as a function of cosine of the SZA. The SNO calibration is obtained from regressing *Aqua* MODIS and AVHRR 50-km coincident radiance pairs during the hemispherical summer. In all cases, a spectral band adjustment factor (SBAF) is applied to account for SRF differences. The SBAFs are based on the regression of *Environmental Satellite* (*Envisat*) Scanning Imaging Absorption Spectrometer for Atmospheric Chartography (SCIAMACHY) pseudoradiance pairs, derived from the convolution of invariant target–specific hyperspectral top-of-the-atmosphere (TOA) radiances with the target and reference sensor SRFs (Scarino et al. 2016). This study utilizes observations taken over the Libya-1, Libya-4, Arabia-1, and Niger-1 pseudoinvariant calibration sites (PICS; Cosnefroy et al. 1996). These combined PICS observations are referred to as the desert invariant target. Similarly, the combined Dome-Concordia (Dome-C) and Greenland PICS observations are referred to as the polar ice invariant target. The DCC invariant target calibration method is a large-ensemble statistical approach that relies on interannual consistency of the spatial and seasonal distributions of all identified pixel-level DCC over the tropical ($\pm 15°$ latitude) domain. For convenience, DCC are also referred to as an invariant target. The individual desert or polar ice PICS calibration gains are combined by the inverse variance weights of their temporal variability in order to optimize the resulting calibration stability. The invariant target gains are combined in the same manner and are referred to as the multiple invariant targets referenced to *Aqua* MODIS (MITRAM) calibration approach.

The MITRAM AVHRR calibration coefficients and their associated uncertainty values are provided in section 2. Section 2 also examines the temporal stability of the individual PICS, as well as the calibration consistency among the invariant targets and the *Aqua*-MODIS SNO methods. The intersensor MITRAM calibration consistency is evaluated over the DCC, Libya-1, Libya-4, and Dome-C PICS in section 3. Section 4 presents comparisons of the MITRAM calibration gains with three other published AVHRR calibration studies. Section 5 details the impact of Global Area Coverage (GAC) AVHRR/3 (*N15* through *MetOp-B*) *dual-gain* count averaging. Section 6 concludes the paper.

2. MITRAM calibration gains

Calibration gains typically vary over time after the instrument is launched. This variation is characterized here as a function of days since launch (dsl), which can be computed from the launch dates listed in Table 1. It is

TABLE 2. Individual satellite m_i used in Eqs. (1) and (2), and their associated uncertainty (U_{MITRAM}; %). The term E_0 ($\mathrm{W\,m^{-2}\,sr^{-1}\,\mu m^{-1}}$) and C_0 are listed. *Aqua*-MODIS s_i and U_{SNO} (%) are also given. Bold text denotes satellites in afternoon orbits. Units of m_0 and s_0, m_1 and s_1, and m_2 and s_2 are $\mathrm{W\,m^{-2}\,sr^{-1}\,\mu m^{-1}}$ per count, $\mathrm{Wm^{-2}\,sr^{-1}\,\mu m^{-1}}$ per count per day, and $\mathrm{Wm^{-2}\,sr^{-1}\,\mu m^{-1}}$ per count per day squared, respectively. The Ct and C_0 units are in 10-bit single-gain counts.

Ch1	E_0	m_0	m_1	m_2	C_0	U_{MITRAM}	s_0	s_1	s_2	U_{SNO}
TIROS-N	**437.60**	**0.5110**	$\mathbf{1.732 \times 10^{-4}}$	$\mathbf{-1.924 \times 10^{-7}}$	**40.0**	**1.9**				
N6	520.13	0.6145	-3.730×10^{-6}	0.0	36.5	2.1				
N7	**523.76**	**0.6188**	$\mathbf{6.083 \times 10^{-5}}$	$\mathbf{-4.020 \times 10^{-7}}$	**35.8**	**1.8**				
N8	523.76	0.6606	6.163×10^{-5}	0.0	39.4	2.0				
N9	**519.60**	**0.5691**	$\mathbf{1.153 \times 10^{-4}}$	$\mathbf{-1.282 \times 10^{-8}}$	**37.9**	**1.7**				
N10	519.60	0.5934	7.244×10^{-5}	-2.800×10^{-8}	34.6	1.9				
N11	**518.52**	**0.5850**	$\mathbf{3.640 \times 10^{-6}}$	$\mathbf{5.260 \times 10^{-9}}$	**40.0**	**1.8**				
N12	515.05	0.6293	4.779×10^{-5}	-7.482×10^{-9}	40.1	2.0				
N14	**515.17**	**0.6237**	$\mathbf{1.038 \times 10^{-4}}$	$\mathbf{-3.149 \times 10^{-8}}$	**41.0**	**1.9**				
N15	522.42	0.6416	-2.540×10^{-6}	2.690×10^{-10}	38.0	2.2	0.6341	8.140×10^{-6}	-1.695×10^{-9}	1.1
N16	**522.82**	**0.5870**	$\mathbf{1.836 \times 10^{-5}}$	$\mathbf{-1.363 \times 10^{-9}}$	**38.9**	**1.9**	**0.5907**	$\mathbf{1.558 \times 10^{-5}}$	$\mathbf{-8.330 \times 10^{-10}}$	**0.7**
N17	520.74	0.6045	2.137×10^{-5}	-2.399×10^{-9}	40.9	1.6	0.6068	2.481×10^{-5}	-4.195×10^{-9}	1.0
N18	**519.86**	**0.5957**	$\mathbf{2.057 \times 10^{-5}}$	$\mathbf{-1.681 \times 10^{-9}}$	**40.0**	**1.5**	**0.5947**	$\mathbf{2.063 \times 10^{-5}}$	$\mathbf{-2.163 \times 10^{-9}}$	**0.7**
MetOp-A	522.21	0.5918	2.721×10^{-5}	-5.927×10^{-9}	41.0	1.6	0.5896	2.220×10^{-5}	-4.167×10^{-9}	0.7
N19	**518.74**	**0.5740**	$\mathbf{1.406 \times 10^{-5}}$	$\mathbf{-2.999 \times 10^{-9}}$	**40.2**	**1.6**	**0.5712**	$\mathbf{1.956 \times 10^{-5}}$	$\mathbf{-5.994 \times 10^{-9}}$	**0.9**
MetOp-B	522.92	0.5849	4.974×10^{-5}	-2.572×10^{-8}	39.7	1.8	0.5808	6.24×10^{-5}	-5.38×10^{-8}	0.6

assumed that the AVHRR visible sensor degradation is gradual and systematic, where the temporal gain change is characterized using a quadratic function. For unusually short records, a linear fit is all that is necessary to describe the change in gain. For each AVHRR sensor, the radiance L ($\mathrm{W\,m^{-2}\,sr^{-1}\,\mu m^{-1}}$) is computed from the calibration gain (m) and the measured single-gain 10-bit count (C) using Eq. (1),

$$L = m(C - C_0), \quad \text{where}$$
$$m = m_0 + m_1 \times \mathrm{dsl} + m_2 \times \mathrm{dsl}^2, \tag{1}$$

where C_0 is the single-gain space count, or offset, and the coefficients m_0, m_1, and m_2 are given in units of $\mathrm{W\,m^{-2}\,sr^{-1}\,\mu m^{-1}}$ per count, $\mathrm{W\,m^{-2}\,sr^{-1}\,\mu m^{-1}}$ per count per day, and $\mathrm{W\,m^{-2}\,sr^{-1}\,\mu m^{-1}}$ per count per day squared, respectively, in which Ct is count. For the AVHRR/3 series, the dual-gain counts are first converted to single-gain counts using the process described in Part I. The radiance is converted to the nominal, or scaled, reflectance (ρ_{scaled}) using Eq. (2),

$$\rho_{\mathrm{scaled}} = L/E_0, \tag{2}$$

where E_0 is the AVHRR band solar constant ($\mathrm{W\,m^{-2}\,sr^{-1}\,\mu m^{-1}}$) and is computed by convolving the AVHRR SRF with the MODIS Characterization Support Team (MCST) solar spectra (Lyapustin et al. 2007; ftp://mcst.ssaihq.com/pub/permanent/MCST/Solar_Irradiance/). The *Aqua* MODIS level 1B calibration reference radiances are determined from the MCST solar spectra from reflectance-based measurements (Xiong et al. 2005).

The MITRAM AVHRR calibration coefficients (m_i) are given in Tables 2 and 3 for channels 1 and 2, respectively, where $i = 0$, 1, or 2. The AVHRR channels 1, 2, and 3a SNO calibration coefficients (s_i) are provided in Tables 2–4, respectively, in the same units as their m_i counterparts. The coefficients s_i are applied by replacing m_i with s_i in Eq. (1). The AVHRR channels 1, 2, and 3a are referenced to *Aqua* MODIS bands 1 and 2, and *Terra* MODIS band 6, respectively. *Terra* MODIS is used as a reference for the AVHRR channel (Ch3a) because *Aqua* MODIS band 6 has too many inoperable detectors (Xiong et al. 2004). Because all AVHRR/3 Ch3a observations were coincident with *Terra* MODIS, no MITRAM calibration was performed for Ch3a. The corresponding MITRAM (U_{MITRAM}) and SNO (U_{SNO}) calibration uncertainty estimates are also provided in the tables and are discussed in the following section. The MITRAM coefficients can also be obtained online (http://www-pm.larc.nasa.gov/cgi-bin/site/showdoc?mnemonic=SATCALIB2&c=home).

The MODIS and AVHRR SNO radiance pair linear regression–derived space count and the space count from the unlit Earth disc (section 2c in Part I) were similar. The SNO space count for Ch1 and Ch2 results validate the unlit Earth disc space count methodology.

a. Uncertainty analysis

The MITRAM AVHRR calibration uncertainty analysis does not take into account scan angle dependency, polarization, or detector noise, but it computes the uncertainties related to the calibration methodology and the sensor degradation. It is the uncertainty expected when

TABLE 3. As in Table 2, but for AVHRR Ch2.

Ch2	E_0	m_0	m_1	m_2	C_0	U_{MITRAM}	s_0	s_1	s_2	U_{SNO}
TIROS-N	**327.80**	**0.4242**	$\mathbf{6.264 \times 10^{-5}}$	**0.0**	**40.0**	**2.4**				
N6	336.09	0.4341	7.290×10^{-5}	0.0	38.3	3.3				
N7	**336.93**	**0.4094**	$\mathbf{7.884 \times 10^{-5}}$	$\mathbf{-2.971 \times 10^{-8}}$	**37.3**	**2.9**				
N8	338.47	0.4777	5.134×10^{-5}	0.0	41.1	3.7				
N9	**335.81**	**0.4019**	$\mathbf{6.008 \times 10^{-5}}$	$\mathbf{-2.590 \times 10^{-8}}$	**39.6**	**2.4**				
N10	334.40	0.4334	2.919×10^{-5}	-9.317×10^{-9}	35.0	3.1				
N11	**337.01**	**0.3902**	$\mathbf{8.870 \times 10^{-5}}$	$\mathbf{-1.938 \times 10^{-9}}$	**39.9**	**3.0**				
N12	336.71	0.4859	3.039×10^{-5}	-5.114×10^{-9}	40.0	3.6				
N14	**330.40**	**0.4952**	$\mathbf{1.005 \times 10^{-5}}$	$\mathbf{3.335 \times 10^{-9}}$	**41.0**	**3.0**				
N15	331.99	0.4583	5.530×10^{-6}	-9.250×10^{-10}	38.7	3.5	0.4312	1.788×10^{-5}	-2.450×10^{-9}	1.5
N16	**329.94**	**0.385**	$\mathbf{8.370 \times 10^{-6}}$	$\mathbf{5.500 \times 10^{-11}}$	**39.3**	**3.3**	**0.3826**	$\mathbf{1.374 \times 10^{-5}}$	$\mathbf{-1.274 \times 10^{-9}}$	**1.4**
N17	329.88	0.4369	2.794×10^{-5}	-5.068×10^{-9}	40.1	2.5	0.4337	3.640×10^{-5}	-7.831×10^{-9}	1.6
N18	**326.33**	**0.403**	$\mathbf{1.671 \times 10^{-5}}$	$\mathbf{-1.573 \times 10^{-9}}$	**39.5**	**2.8**	**0.4062**	$\mathbf{9.270 \times 10^{-6}}$	$\mathbf{8.2 \times 10^{-11}}$	**2.0**
MetOp-A	329.76	0.4215	1.835×10^{-5}	-2.105×10^{-9}	40.1	2.2	0.4259	1.140×10^{-5}	6.0×10^{-12}	1.5
N19	**336.88**	**0.4031**	$\mathbf{1.653 \times 10^{-5}}$	$\mathbf{-2.978 \times 10^{-9}}$	**39.9**	**2.4**	**0.39**	$\mathbf{4.890 \times 10^{-6}}$	$\mathbf{-1.675 \times 10^{-8}}$	**1.9**
MetOp-B	330.50	0.3903	2.489×10^{-5}	0.0	40.0	2.6	0.3853	1.633×10^{-5}	0.0	0.8

analyzing the entire sensor record, not just a few pixels. Because the SNO and PICS calibration methods use only near-nadir pixels, and because the DCC calibration uses pixels within 40° VZA, the user is cautioned when interpreting the MITRAM calibration uncertainties for large scan angles. The MITRAM calibration uncertainty is estimated from a composite of the following parameters: 1) the absolute uncertainty in the reference *Aqua* MODIS calibration, 2) the uncertainty in the MODIS calibration transfer to the *N16* AVHRR sensor, 3) the uncertainty associated with the PICS or DCC DM, and 4) and the variance of the monthly MITRAM gains computed from a second-order temporal trend derived over the given satellite record. We assumed these sources of uncertainty are independent of each other and summed them in quadrature to compute the overall uncertainty. The calibration trend detection confidence is based on the PICS-observed natural variability, the length of the record, and the magnitude of the expected trend (Weatherhead et al. 1998). Longer satellite records reduce the impact of the residual temporal variability embedded in the trend.

The *Aqua* MODIS calibration uncertainty has been estimated at 1.65%, 1.67%, and 1.91%, for bands 1 (0.65 μm), 2 (0.86 μm), and 6 (1.6 μm), respectively (Xiong et al. 2005). This is the lower bound of the *Aqua* MODIS uncertainty established by known prelaunch uncertainties. The *Aqua* MODIS C6 calibration temporal stabilities for bands 1 and 2 are within 1%, but they are smallest during the early record (Doelling et al. 2015). It is also known that the scan mirror angle of incident reflectance changes over time, and is monitored and corrected using the approach of Sun et al. (2014). This correction may cause a slight difference in the calibration reference between the near-nadir desert, polar ice, and SNO observations, and the DCC observations that are within a 40° viewing angle range.

The *Aqua* MODIS–to–*N16* AVHRR calibration transfer uncertainty (U_{SNO}) is then the monthly SNO gain temporal variability, or standard error (StdErr),

TABLE 4. Individual satellite *Aqua* MODIS SNO calibration coefficients (s_x) and (U_{SNO}) (%) for AVHRR band 3a (1.61 μm). Both E_0 (W m^{-2} sr^{-1} μm^{-1}) and C_0 are listed. The coefficients are valid for the time ranges in Table 1, unless otherwise indicated. Bold text denotes satellites in afternoon orbits. Units of s_0, s_1, and s_2 are W m^{-2} sr^{-1} μm^{-1} per count, W m^{-2} sr^{-1} μm^{-1} per count per day, and W m^{-2} sr^{-1} μm^{-1} per count per day squared, respectively. Ct is a brightness count. The Ct and C_0 units are in 10-bit single-gain counts.

Ch3a	E_0	s_0	s_1	s_2	C_0	U_{SNO}
N16[a]	**78.143**	**0.075 23**	$\mathbf{5.739 \times 10^{-7}}$	**0**	**38.3**	[b]
N17	78.199	0.089 46	3.452×10^{-6}	-3.916×10^{-10}	39.4	0.6
N18[c]	**78.276**	**0.0904**	**0**	**0**	**37.0**	[b]
MetOp-A	78.279	0.087 31	5.599×10^{-6}	-3.504×10^{-10}	36.0	1.7
MetOp-B[d]	78.094	0.08249	1.959×10^{-5}	0	39.4	[b]

[a] Valid during 2001 and 2002.
[b] Records too short to compute uncertainty.
[c] Valid during July 2005.
[d] Valid during 2013 and 2014.

with respect to the quadratic fit, having values of 0.7% and 1.4% for bands 1 and 2, respectively (Fig. 5b in Part I). The SNO gains are computed monthly to reduce the impact of the individual SNO radiance pair matching noise, as well as to provide a large dynamic range for computing the gain. The radiance pair noise with respect to the monthly linear regressions also contains the variability due to the spectral band differences induced by changing atmospheric conditions during the month. The mean atmospheric conditions/effects, such as clouds, aerosol, Rayleigh scattering, water vapor, ozone, and other absorptive gases, as well as the surface spectral reflectance, are captured by the seasonal SCIAMACHY-based SBAFs. Aerosols, Rayleigh scattering, water vapor, and ozone corrections are not computed explicitly for each instantaneous observation. The SBAF uncertainty, which is the slope uncertainty of the SCIAMACHY-convolved *N16* AVHRR–MODIS pseudoradiance pairs, is 0.06% and 0.04% for bands 1 and 2, respectively (Fig. 4 in Part I). The SBAF uncertainty is included in U_{SNO}.

The desert and polar ice PICS DM uncertainty [U_{PICS}(DM)] is estimated as the standard error of the quadratic regression from *N16* monthly mean observed AVHRR radiances as a function of the cosine of the SZA (μ_0). The *N16* Libya-4 PICS DM uncertainty is 1.3% and 4.1% for Ch1 and Ch2, respectively (Fig. 7 in Part I). Adding the AVHRR 11-μm minus 12-μm brightness temperature difference (BTD) to estimate the precipitable water (PW) in order to account for the near-infrared (NIR) water vapor absorption in Ch2 (Yu and Wu 2010) reduces the DM uncertainty from 4.1% to 2.9%. For AVHRR/1 sensors without a 12-μm channel, no Ch2 water vapor (WV) adjustment is performed. For Dome-C, the uncertainty is 2.0% and 2.5% for Ch1 and Ch2, respectively (Fig. 8 in Part I). Owing to the dry and cold conditions over Dome-C, no PW BTD term was utilized. Since the observed SCIAMACHY hyperspectral radiances capture the mean SBAF conditions over the PICS, the SBAF uncertainty for each PICS is equivalent to the uncertainty of the *N16* and AVHRR target instrument SCIAMACHY pseudoradiance pair regression slope uncertainty. No significant seasonal SCIAMACHY-based desert PICS SBAF differences were found between *N16* Ch2 and other AVHRR Ch2 sensors, owing to the similarity of the SRFs. The SBAF uncertainty is included in the U_{PICS}(DM).

The DCC DM uncertainty [U_{DCC}(DM)] of 0.76% is based on the standard error of the polynomial fit of the *N16* DCC monthly observed reflectance modes as a function of μ_0 (Fig. 9b in Part I). The DCC mode reflectance also depends on the AVHRR 11-μm brightness temperature (BT) threshold. Doelling et al. (2013) found that the DCC mode reflectance decreases by 0.5% if the MODIS BT threshold is increased from 200 to 205 K. Mittaz and Harris (2011) found that the *MetOp-A* AVHRR BT biases are less than 0.5 K when compared with the Infrared Atmospheric Sounding Interferometer (IASI), and are remarkably stable over time. Assuming a doubling of the temperature bias (or a 1-K departure) from Mittaz and Harris (2011), which may be the case for the pre-IASI record, suggests a 0.1% DCC mode reflectance bias or uncertainty. Because the *Aqua* MODIS Ch2 radiances saturate for DCC scenes or conditions, the observed AVHRR Ch2 radiance is converted to a Ch1-equivalent radiance by applying a DCC SBAF. For DCC, the SBAF uncertainty is based on the *N16* AVHRR Ch1 and target satellite Ch2 SCIAMACHY pseudoradiance pair slope uncertainty. For Ch1 the DCC temperature threshold uncertainty and the Ch1 SBAF are included in U_{DCC}(DM), and for Ch2 both the DCC temperature threshold uncertainty and the Ch1-to-Ch2 SBAF is included in U_{DCC}(DM).

A quadratic fit is computed from the monthly gains to estimate the PICS calibration trend over time. The temporal standard error (σ) relative to the quadratic fit is then the uncertainty resulting from the natural variability of the PICS, which intrinsically includes the methodology noise and departures from the mean SBAF conditions. The PICS calibration uncertainty (U_{PICS}), with respect to the *Aqua* MODIS C6 calibration reference, is computed using Eq. (3),

$$U_{\mathrm{PICS}} = \sqrt{U^2(\mathrm{SNO}) + U^2_{\mathrm{PICS}}(\mathrm{DM}) + \sigma^2_{\mathrm{PICS}}} \qquad (3)$$

where U(SNO) and U_{PICS}(DM) are the SNO and PICS DM uncertainty, respectively. The combined desert monthly gain (g_{comb}) time series is computed from weighting factors (w_i) based on the inverse of the variance ($1/\sigma_i^2$) using the individual PICS monthly gains (g_i) and Eq. (4),

$$g_{\mathrm{comb}} = \Sigma g_i w_i, \quad \text{where} \quad w_i = (1/\sigma_i^2)/(\Sigma 1/\sigma_i^2). \qquad (4)$$

A quadratic fit [Eq. (1)] is then applied to the combined desert monthly gains from which the σ_{desert} is computed. The desert DM uncertainty [U_{desert}(DM)] and desert calibration uncertainty (U_{desert}) are computed using Eq. (5),

$$U_{\mathrm{desert}} = \sqrt{U^2(\mathrm{SNO}) + U^2_{\mathrm{desert}}(\mathrm{DM}) + \sigma^2_{\mathrm{desert}}},$$
$$\text{where} \quad U_{\mathrm{desert}}(\mathrm{DM}) = \sqrt{\sum_i^{4\mathrm{PICS}} w_i U_i^2(\mathrm{DM})}. \qquad (5)$$

Similarly, the desert, polar ice, and DCC monthly gains are regressed using a quadratic fit to compute σ_{MITRAM}.

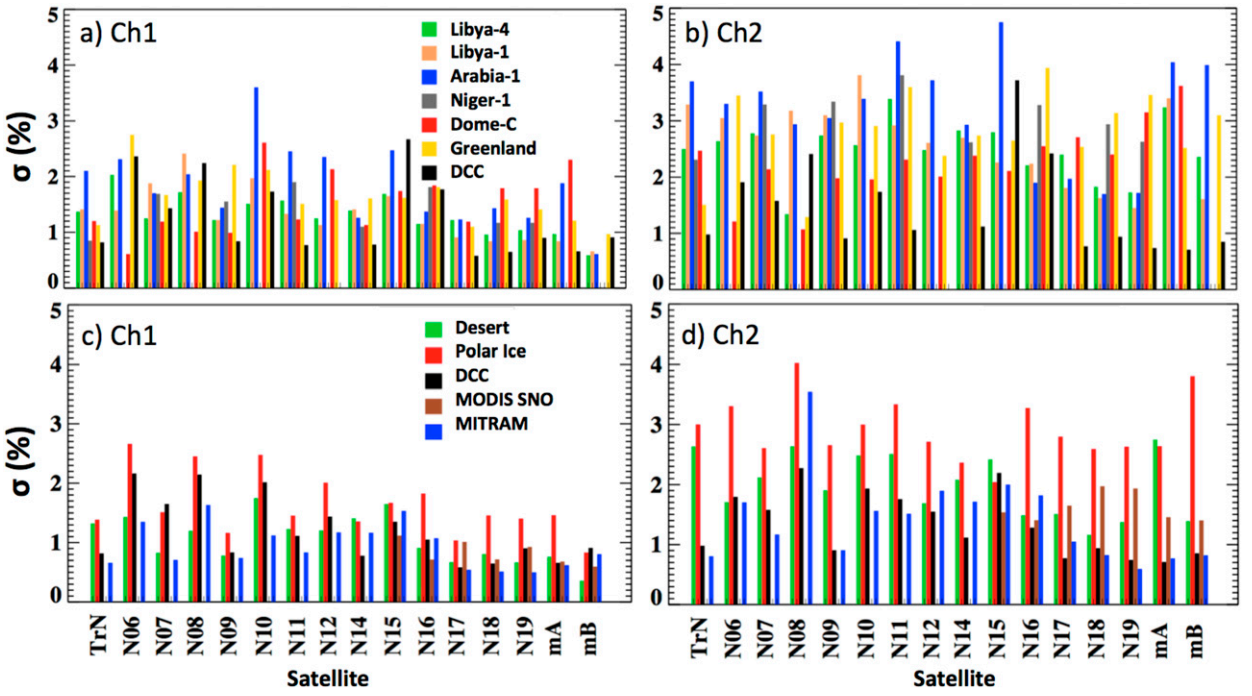

FIG. 1. Individual PICS σ (%) values for AVHRR (a) Ch1 and (b) Ch2. Individual invariant target σ (%) values for AVHRR (c) Ch1 and (d) Ch2. Niger-1 not shown for morning-orbit sensors.

The MITRAM DM uncertainty [U_{MITRAM}(DM)] is computed from the three individual invariant target DM uncertainties [U_i(DM)] weighted (w_i) using the individual invariant target σ in Eq. (4). The MITRAM calibration uncertainty (U_{MITRAM}), with respect to the *Aqua* MODIS C6 calibration reference, is computed using Eq. (6),

$$U_{\mathrm{MITRAM}} = \sqrt{U^2(\mathrm{SNO}) + U^2_{\mathrm{MITRAM}}(\mathrm{DM}) + \sigma^2_{\mathrm{MITRAM}}},$$
$$\text{where} \quad U_{\mathrm{MITRAM}}(\mathrm{DM}) = \sqrt{\sum_{i}^{3\mathrm{targets}} w_i U_i^2(\mathrm{DM})}. \tag{6}$$

Tables 2 and 3 list the values of U_{MITRAM} and U_{SNO} for Ch1 and Ch2, respectively, for each AVHRR copy. Similarly, Table 4 presents the AVHHR/3 Ch3a U_{SNO} values. All of the AVHRR Ch1 U_{MITRAM} values are between 1.5% and 2.2%. The AVHRR Ch2 U_{MITRAM} values are between 2.2% and 3.7%. Values of the morning sensor U_{MITRAM} for both channels are greater than those of the afternoon sensors. These results are expected given that the 0730 LT and near-terminator orbit oblique sun angle observations over the PICS have very low signal-to-noise ratios. The larger Ch2 U_{MITRAM} values, relative to those of Ch1, are mainly due to NIR water vapor absorption and surface moisture/vegetation variability, which has a larger impact on the Ch2 reflectance. The U_{MITRAM} exceeds U_{SNO} because the U_{MITRAM} incorporates the U_{SNO} term, as well as the DM uncertainty and σ terms in Eq. (6). However, the U_{SNO} values may be underestimated because Eq. (6) does not account for the *Aqua* MODIS on-orbit calibration fluctuations. The MODIS calibration fluctuations are embedded in the PICS DM and would increase the DM uncertainty. To obtain a consistent calibrated AVHRR 36-yr record, the SNO calibration during the AVHRR/3 era should not be combined with the MITRAM calibration during the AVHRR/1/2 eras.

b. *PICS stability*

This study relies on the combined stability of several PICS to minimize the impact of natural variability for any single invariant target. For example, deserts may have rain events that can cause reflectance anomalies lasting for several months (Yu et al. 2014). In weighting the individual PICS by the inverse of their temporal variability, the most stable PICS would dominate the calibration. Also, if a PICS reflectance signature were constantly drifting, then the method would prevent the PICS reflectance from degrading the MITRAM calibration.

Figures 1a and 1b display the individual PICS σ values based on the monthly gain scatter about the individual

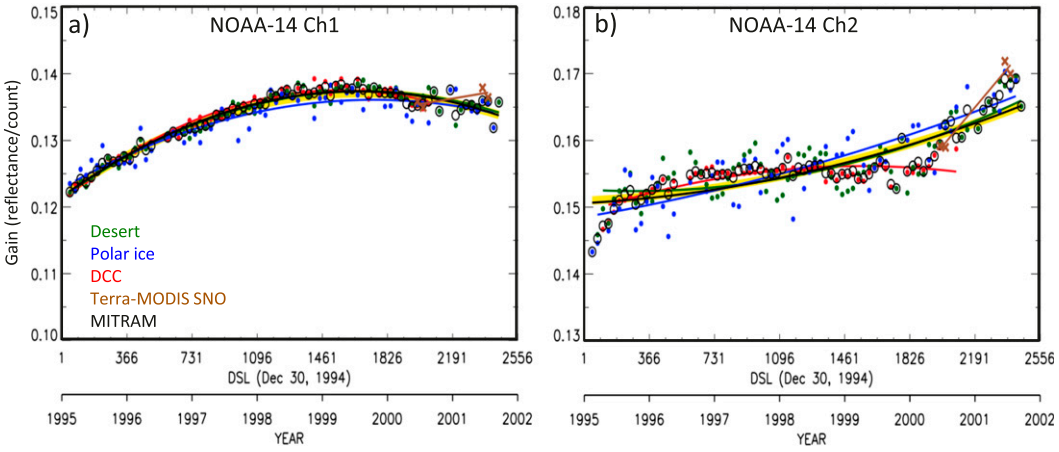

FIG. 2. Monthly nominal reflectance gains and associated quadratic fit regression lines for *N14* AVHRR (a) Ch1 and (b) Ch2 for desert (green), polar ice (blue), DCC (red), *Terra* MODIS SNO (brown), and MITRAM (black). Thick yellow line represents the quadratic regression fit achieved by combining all time-overlapped invariant target monthly gains weighted by the individual invariant target inverse of the variance.

quadratic fits. The Niger-1 TOA reflectance variability observed by the 0730 LT satellite instruments is very large, and therefore the site is not used for their calibration. It is important that the desert PICS not only maintain stable surface reflectance values but also have a consistently dry atmosphere. The Niger-1 PICS is close to the intertropical convergence zone, where the column water vapor can vary substantially. The polar ice targets have the greatest σ of all the PICS. For Ch2, the Dome-C TOA reflectance is more stable than Greenland due to the dry atmosphere associated with the interior of the Antarctica Plateau.

Figures 1c and 1d summarize the desert, polar ice, DCC, and MITRAM σ values. For deserts, the combined PICS monthly gains result in a lower σ than that from any individual PICS. This result confirms that an individual PICS with a large σ does not adversely impact the combined invariant target stability. This is not the case for the polar ice case. Because the Greenland or Dome-C PICS can be observed only within the few months surrounding their respective summer solstices, the PICS measurements do not overlap. The PICS gains are simply inserted into the combined polar ice record, and all monthly gains are weighted equally when computing σ. In general, the MITRAM σ is lower than either the desert or polar ice value. The DCC σ is perhaps less than that of the MITRAM value because the DCC record is limited to observations for SZA less than 68°, whereas larger SZAs have greater temporal noise. The SNO and MITRAM gains have similar σ values for Ch1. For Ch2, however, the MITRAM σ is less than that for the Ch2 SNO, except in the case of *N15* and *N16*. This result suggests that the calibration trend confidence derived from the MITRAM coefficients should be similar to or better than that of the SNO. The MITRAM σ values over the entire AHVRR record are within 1.5% and 2.0% for Ch1 and Ch2, respectively, except for *N8* Ch2.

c. *PICS and SNO calibration consistency*

Consistency among the independent invariant target calibrations validates the MITRAM approach. This self-validation can be accomplished by comparing the MITRAM trend with the individual invariant target trends as shown in Fig. 2. The circles represent the monthly MITRAM gains, which are computed according to Eq. (4). The thick solid black line is the resulting MITRAM trend. A similar trend (thick yellow line) is produced if the PICS overlapping time record gains are simply given the same weights before regression is performed. The monthly MITRAM gains can then be used to determine the shape of the trend rather than assume a quadratic trend. It appears that for *N14* Ch2, the quadratic trend inadequately describes the true trend, especially during the year 2000. This apparent year 2000 feature is present for all invariant targets, with the exception of polar ice. The sharp increase in the trend is validated with the SNO gains from *Terra* MODIS, which was available after January 2000. The *Terra* MODIS radiances were scaled to *Aqua* MODIS using factors of 1.017 and 1.001 for Ch1 and Ch2, respectively (Doelling et al. 2015). When a third-order fit is applied, the MITRAM standard error is reduced from 1.86% to 0.67% (not shown). The third-order fit also captures the sudden gain increase during 1995. Future calibration efforts will determine the optimal polynomial fit that best fits the true calibration drift.

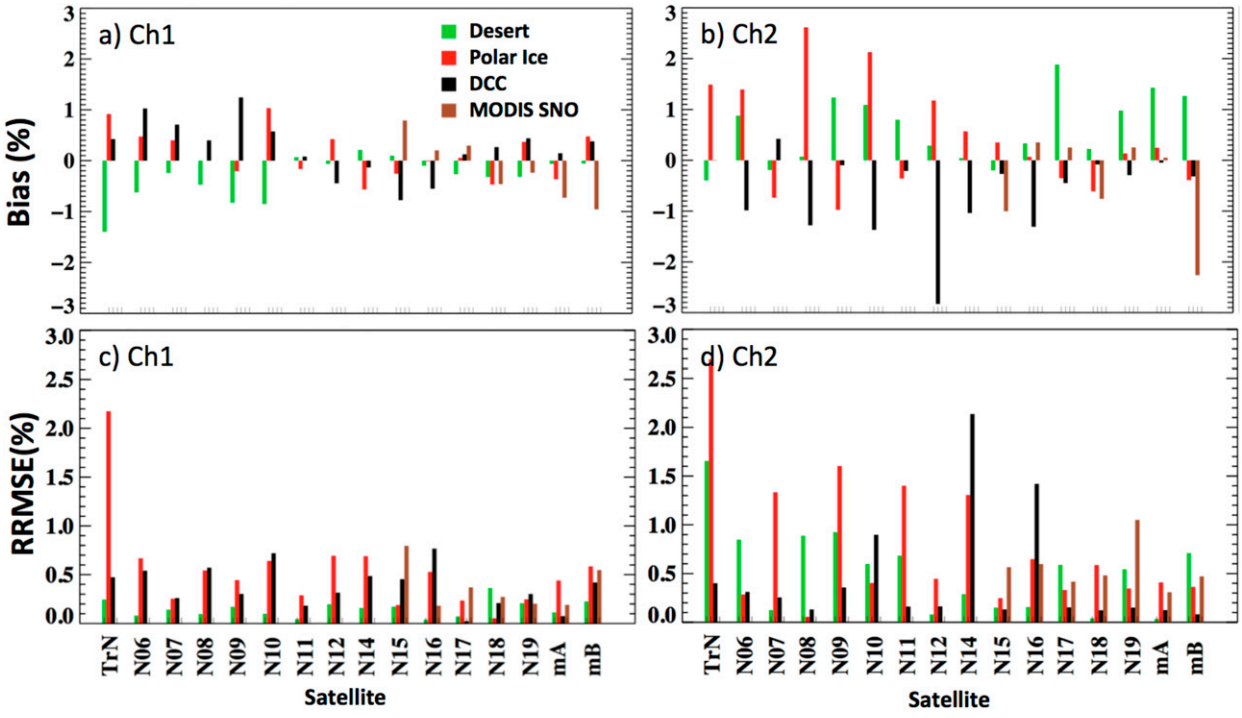

FIG. 3. Individual invariant target minus MITRAM relative calibration bias (%) computed from their respective quadratic fits (%) for AVHRR (a) Ch1 and (b) Ch2. The individual invariant target minus the MITRAM monthly gain RRMSE (%) after removing the relative calibration bias for AVHRR (c) Ch1 and (d) Ch2.

Each individual target calibration provides both the transfer of the *Aqua* MODIS calibration reference and the relative sensor degradation over time. The invariant target calibrations are therefore compared to MITRAM using the relative calibration bias (RCB) over the record and the trend difference. The trend difference is defined as the relative RMS error (RRMSE) of the invariant target minus the MITRAM monthly gains computed from the quadratic fits after removing the RCB. The DCC record is valid only for SZA $< 68°$ and for the *N14* record ending during the year 2000 (Fig. 2). Also for many NOAA morning orbits, the DCC record is only half of the overall record. The RCB and the RRMSE are shown in Fig. 3.

The invariant target RCB consistency with MITRAM is mostly within 1% and 2% for Ch1 and Ch2, respectively (Figs. 3a and 3b). This consistency implies that all invariant targets are valuable for transferring the MODIS reference calibration. One possibility for the large *N9* Ch1 and *N12* Ch2 DCC RCB may be a result of inconsistent cross-sensor BT at 205 K, which are used to identify DCC pixels (see section 2a), and will need further investigation. Overall, the invariant target trends are mostly consistent to within 0.75%, 1.75%, and 0.75%, with MITRAM for Ch1, AVHRR/1/2 Ch2, and AVHRR/3 Ch2, respectively (Figs. 3c and 3d), suggesting that all invariant targets are accurately defining the sensor on-orbit calibration drift. In general, the invariant target trend consistency is greater than the calibration bias consistency; that is, it is easier to determine the relative sensor degradation rather than the magnitude of the calibration gain.

The SNO and MITRAM relative calibration differences agree within 1% for Ch1 and Ch2 (Figs. 3a and 3b), except for *MetOp-B* Ch2, which is due to the 2-yr record not being long enough to mitigate the residual seasonal variability about the invariant target and SNO trends. The SNO and MITRAM RRMSE values are consistent to within 0.75% for both channels, except for *N15* Ch1 and *N19* Ch2 (Figs. 3c and 3d). This consistency suggests that the MITRAM calibration can nearly replicate the MODIS SNO calibration.

3. AVHRR record PICS reflectance time series

The PICS used in this study are temporally stable to within 1.3% over 13 years based on *Aqua* MODIS band 1 observations (Fig. 6 in Part I). The *Aqua* MODIS calibration relies on solar diffuser and lunar observations to maintain on-orbit calibration stability. The MITRAM AVHRR calibration gains can be evaluated for discontinuities and stability across overlapping

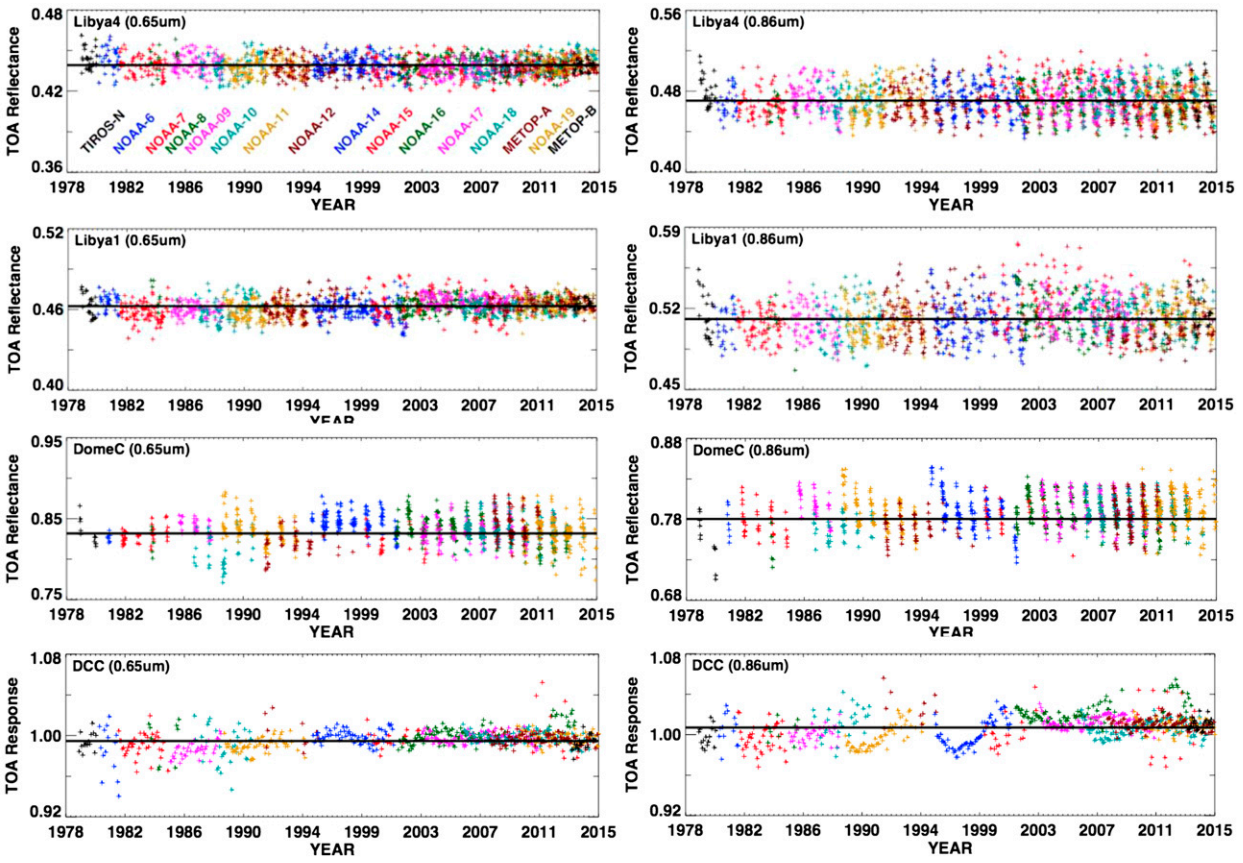

FIG. 4. AVHRR multisensor ρ_{norm} color coded by sensor platform for (left) Ch1 and (right) Ch2. The black lines represent the 36-yr ρ_{norm} mean.

sensor records referenced to the temporal stability of the PICS. This evaluation can be accomplished if the PICS near-nadir observed radiances are normalized to a common μ_0 and spectral band. The observed sensor reflectances are spectrally adjusted to the *N16* AVHRR SRF based on the PICS-specific SBAF and to a common SZA of 30°, 30° and 65° for DCC, desert, and polar ice targets respectively, using the *N16* DM to provide an observed sensor normalized reflectance (ρ_{norm}). This overall adjustment is accomplished using Eq. (7),

$$\rho_{\text{norm}} = \left[\frac{m(C - C_0)}{E_{\text{SUN}}\gamma(d)\mu_0}\right] \text{SBAF}\left[\frac{\text{DM}(\mu_0)}{\text{DM}(\mu_{\text{OBS}})}\right], \qquad (7)$$

where C is the observed single-gain count, C_0 is the space count, m is the MITRAM gain from Eq. (1), E_{SUN} is the *N16* band solar radiance, $\gamma(d_y)$ is the Earth–sun distance correction ratio as a function of day of year, and μ_{OBS} is the observed μ. For DCC, C is the monthly PDF mode single-gain count.

Figure 4 displays the Libya-1, Libya-4, Dome-C, and DCC ρ_{norm} for Ch1 and Ch2 color coded by the AVHRR sensor. The 36-yr (1978–2014) ρ_{norm} mean, which is the average of all sensor ρ_{norm} results, is plotted as the solid black horizontal line. The ρ_{norm} variability is the combined effect of the invariant target natural variability and inadequate sensor DM and SBAF models. The target natural variability can be identified if all sensor ρ_{norm} values track similarly, whereas diverging ρ_{norm} values indicate issues with the sensor models. For the Libyan deserts and DCC, ρ_{norm} appears to be stable over the AVHRR record, whereas the Dome-C ρ_{norm} values indicate several multiyear anomalies. It seems that the Dome-C variability is owed to the combination of both target variability and inadequate sensor models. Some of the Dome-C ρ_{norm} results appear to be stratified by morning (*N8*, *N10*, and *N12*) and afternoon (*N9*, *N11*, and *N14*) sensors, which points to deficiencies in the DM. The lack of any obvious anomalies during 1991 and 1993 between invariant targets suggests that the stratospheric aerosol loading from the June 1991 Mt. Pinatubo eruption had minimal impact on the MITRAM calibration.

This analysis can also be employed to evaluate the efficacy of applying sensor-specific SBAFs to the

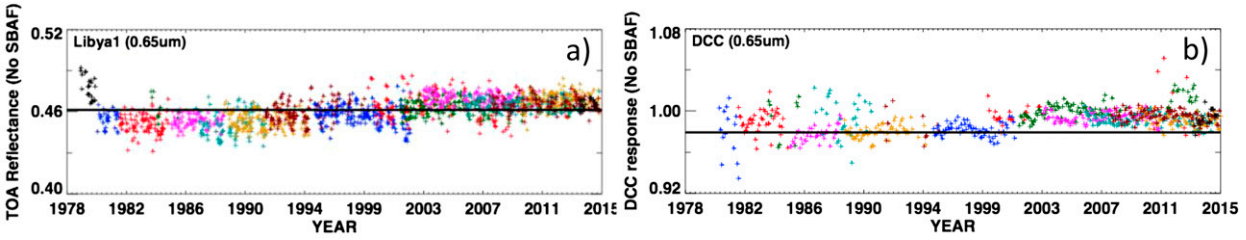

FIG. 5. AVHRR multisensor time series of Ch1 normalized reflectances ρ_{norm} without the SBAF term in Eq. (3) and color coded by sensor platform for (a) Libya-1 and (b) DCC. The black lines represent the 36-yr ρ_{norm} mean with the SBAF term applied and are the same as the line in Fig. 4 in order to facilitate comparison with Fig. 4. Note the greater Libya-1 and DCC without SBAF ρ_{norm} variability, when compared with Fig. 4. The DCC TIROS-N DCC responses are not within the range of (b) and have responses of ~0.80.

invariant targets. The use of the SBAF term in Eq. (7) should reduce the sensor-specific ρ_{norm} bias with respect to the 36-yr mean. Figure 5 shows the AVHRR Ch1 ρ_{norm} computed without the SBAF term in Eq. (7). The 36-yr mean (with SBAF) line is also shown, which represents the same line in Fig. 4. The two examples in Fig. 5 are for Libya-1 and DCC, which, of all analyzed targets and sensors, show the greatest inconsistencies without the SBAF adjustment. There is an apparent reflectance discontinuity between the AVHRR/1/2 and AVHRR/3 series, which is expected given that the SRFs are similar for instruments within each series but they differ between series (Fig. 3 in Part I). The reflectance discontinuities in Fig. 5 (without SBAF) are absent in Fig. 4 (with SBAF), verifying the importance of using the SBAF adjustment.

The ρ_{norm} means for each sensor were subtracted from the 36-yr ρ_{norm} average and are shown as dots in Fig. 6. The bars represent one standard deviation (1σ) of the ρ_{norm} values for each sensor about their average. The DCC ρ_{norm} values are less variable than their PICS counterparts, especially for Ch2, because they are spectrally uniform for wavelengths less than 1 μm and are above the atmospheric water vapor column (Doelling et al. 2012). In general, the ρ_{norm} means for each instrument are within 1% and 2% of the 36-yr average for Ch1 and Ch2, respectively, except for some sensors over Dome-C. Most of the sensor ρ_{norm} standard deviations encompass the 36-yr mean across all invariant targets.

4. Comparison with other AVHRR studies

It is beyond the scope of this study to compare the present results with all published AVHRR calibration studies. Before the advent of the well-calibrated MODIS, AVHRR was the primary instrument for cloud, radiation, and land-use retrievals, which necessitated many calibration studies. A number of historical efforts tried to reconcile the differences among the AVHRR calibration methods (Che and Price 1992; Molling et al. 2010). Recently, several AVHRR calibration studies have applied uniform calibration techniques over the AVHRR record to produce long-term climate records.

Three studies, which utilized consistent calibration methods and reference calibration across numerous satellite platforms, were selected for comparison. 1) Heidinger et al. [2010; Pathfinder Atmospheres–Extended (PATMOS-X)] calibrated the entire AVHRR

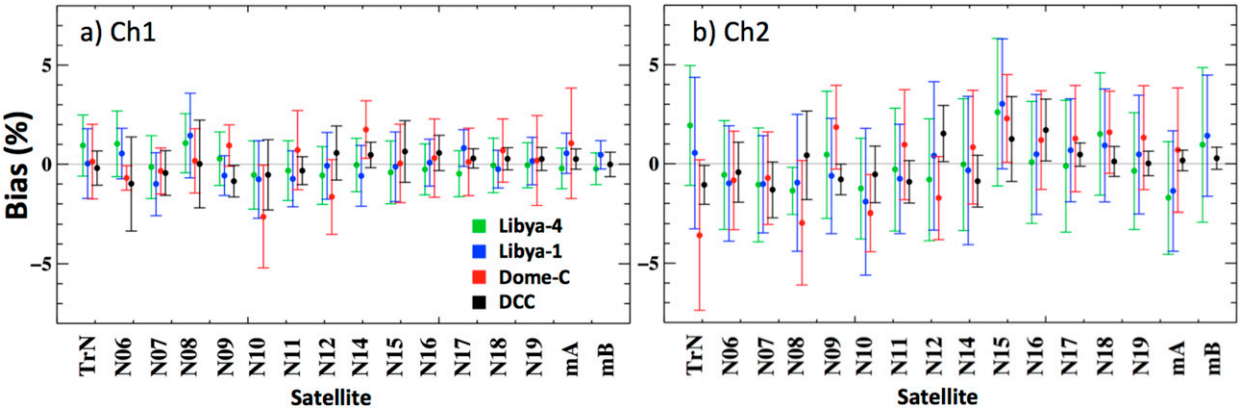

FIG. 6. PICS ρ_{norm} sensor mean bias (%; dot) and the ±1 standard deviation (%) with respect to the 36-yr multisensor mean (black horizontal dotted line) for (a) Ch1 and (b) Ch2.

TABLE 5. Critical components of studies used in the comparisons. *Targets* are the invariant targets and calibration methods used for each study. *Reference* denotes the calibration reference source; the relative departure from the *Aqua*-MODIS C6 calibration is given in parentheses for Ch1 and Ch2, respectively. *SBAF* denotes the spectra source used to compute the SBAFs. *WV* is the column water vapor source used to account for atmospheric absorption variations among the different spectral bands.

Study	Targets	Reference	SBAF	WV
PATMOS-X	MODIS/AVHRR SNO, Libya-4, Dome-C, AVHRR AM/PM SNO	MODIS C5 (<0.2%)[a]	MODTRAN	NCEP reanalysis MODIS NIR bands
Li	6 North African deserts, Dome-C	SeaWiFS (−4.5%, −2.8%)[b]	MODTRAN (−0.5%, −1.5%)[c]	ERA-Interim
STAR	Libya-4	Aircraft (<−5%, <−5%)[d]		
MITRAM	4 desert, Greenland, Dome-C, DCC	*Aqua*-MODIS C6	SCIAMACHY	Desert DM: Ch2 11–12-μm BT

[a] Figures 17 and 19 in Sun et al. (2012); the 2004 *Terra* or *Aqua*-MODIS C5 minus C6 nadir difference during 2004.
[b] Table 6 in Eplee et al. (2011); SeaWiFS/*Aqua*-MODIS bias.
[c] Figure 6 in Li; SBAF comparison with Hyperion.
[d] Heidinger et al. (2002); *N9* and MODIS were within 5%.

record through 2008 using MODIS/AVHRR SNOs, AVHRR morning (AM) and afternoon (PM) satellite SNOs, Libya-4, and Dome-C PICS, which were all referenced to the MODIS Collection 5 calibration. 2) Li et al. (2014, hereafter Li) calibrated the complete AVHRR record using six African deserts and the Dome-C PICS by referencing to the Sea-Viewing Wide Field-of-view Sensor (SeaWiFS) absolute calibration. 3) The NOAA Center for Satellite Applications and Research (STAR) AVHRR/3 operational calibration coefficients were obtained online (http://www.star.nesdis.noaa.gov/smcd/spb/fwu/homepage/AVHRR/Op_Cal_AVHRR/Op_Cal_AVHRR.html), based on Wu et al. (2010; STAR). The STAR AVHRR/1/2 coefficients are obtained from Nagaraja Rao and Chen (1995) for *N7*, *N9*, and *N11*, and from Nagaraja Rao and Chen (1999) for *N14*, using the procedure described by Nagaraja Rao et al. (1994). The STAR calibration is referenced to congruent aircraft measurements with *N9* over White Sands, New Mexico (Smith et al. 1998). The STAR calibration uses the Libya-4 PICS to transfer the *N9* calibration to other AVHRR sensors. The newly updated International Satellite Cloud Climatology Project (ISCCP) calibration coefficients (Rossow and Ferrier 2015) were not considered because they are based on the average of the original ISCCP and PATMOS-X calibration gains. Furthermore, the original ISCCP and PATMOS-X calibrations have already been compared by Rossow and Ferrier (2015). The calibration methods of each study are listed in Table 5.

Figure 7 shows the *N18* AVHRR monthly calibration gains from the three studies along with the MITRAM gain. The slight curvature of the PATMOS-X gains is due to the short, 4-yr record used to derive the quadratic regression coefficients. The STAR real-time gain procedure requires a record of at least one year in length to remove the seasonal bidirectional reflectance distribution function (BRDF) effects of the Libya-4 PICS

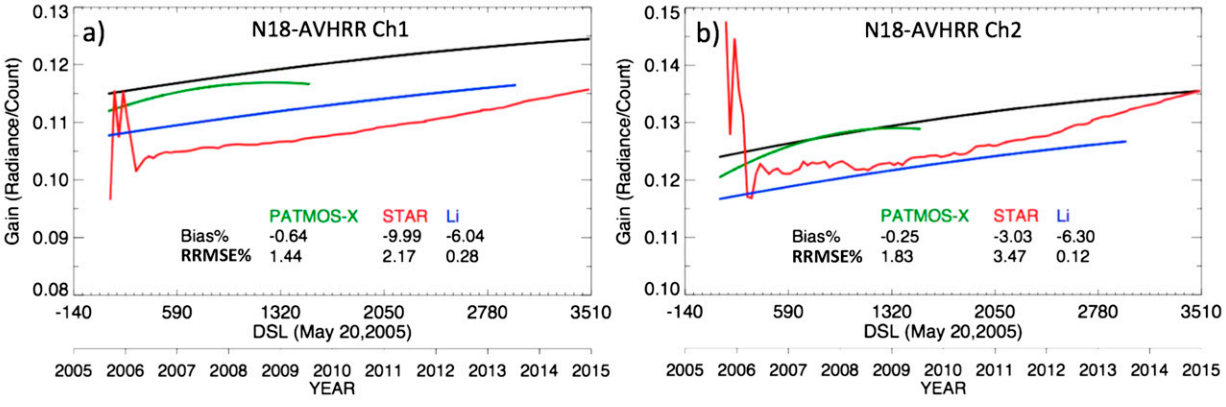

FIG. 7. *N18* AVHRR MITRAM (black line), PATMOS-X (green line), STAR (red line), and Li (blue line) calibration trends for (a) Ch1 and (b) Ch2. The relative calibration bias (%) for each study with respect to MITRAM and the corresponding RRMSE (%) of the monthly gains after removing the relative calibration bias are also shown.

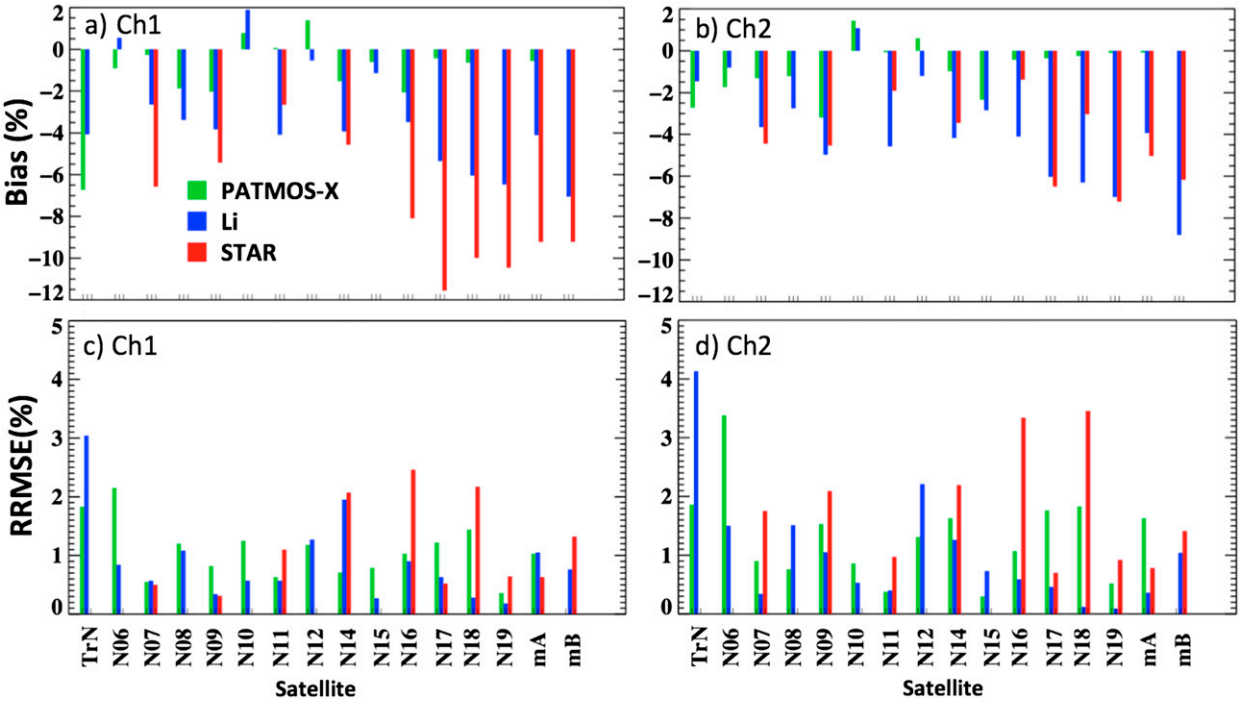

FIG. 8. Calibration gain bias (%) relative to MITRAM for PATMOS-X, Li, and STAR for each AVHRR (a) Ch1 and (b) Ch2. The corresponding RRMSE (%) of the monthly gains with respect to MITRAM after removing the relative calibration bias are also shown for AVHRR (c) Ch1 and (d) Ch2.

(Wu et al. 2010). Following this initial year, the STAR operational calibration stabilizes. Results indicate that the STAR gain increases relative to that of both the Li and MITRAM calibrations after 2013, especially for Ch2, when the satellite enters a near-terminator orbit. The Li and MITRAM gains are parallel to each other for both channels.

a. Calibration reference differences

The PATMOS-X, Li, and STAR calibration coefficients are compared with the MITRAM gains in the same manner as described in section 2c, that is, by separating the RCB and trend difference. Figures 8a and 8b show the RCB for each of the three studies and MITRAM during their overlapping periods. The applicable MITRAM overlapping period extends to 2009 for PATMOS-X, 2013 for Li, and 2014 for STAR. Table 5 lists the study calibration reference sources and the expected relative calibration differences with respect to the *Aqua* MODIS C6 calibration reference. Because both MITRAM and PATMOS-X use MODIS as their calibration reference, the mostly small (0.5%) calibration difference is not surprising. Even for AVHRR/1/2, the PATMOS-X and MITRAM gain differences are less than 2%, except for TIROS-N and *N9* Ch2.

The STAR calibration is referenced to aircraft measurements. The aircraft-minus-PATMOS-X measurements during 1986 and 1987 yield −3% (Rossow and Ferrier 2015, their Fig. 1). The PATMOS-X *N9* Ch1 minus MITRAM calibration difference is −2% (Fig. 8a) and produces a total aircraft minus MITRAM calibration difference of −5%. Heidinger et al. (2002) report that the STAR and MODIS calibration difference is less than 5%. Most AVHRR1/2 sensor STAR and MITRAM calibration differences are between −6% and −2% (Fig. 8) for Ch1. STAR then changed its operational calibration procedure for AVHRR/3 sensors by accounting for the seasonal cycle of Libya-4 reflectances (Wu et al. 2010). This change reduced the calibration reference for Ch1 to −10% with respect to MODIS, a fact noted by Cao et al. (2008) and Wu et al. (2013a). For the STAR Ch2 approach, the calibration difference is between −1% and −5% with respect to MITRAM. The *N16* and *N18* Ch2 calibrations are an exception for which the gain difference is −5% at the beginning of the record, and as the orbits drift toward the terminator the trend increases and eventually exceeds the MITRAM gain (see Fig. 7).

The Li calibration is referenced to the SeaWiFS calibration. Eplee et al. (2011) compared SeaWiFS and MODIS lunar measurements and noted that *Aqua* MODIS bands 1 and 2 were 4.6% and 2.8% brighter than SeaWiFS bands 6 and 8, respectively. Li mentions that the inconsistency with the PATMOS-X calibration

is a result of their inadequate PICS BRDFs and SBAFs. The Li PICS BRDFs were characterized by SeaWiFS measurements. Li compared the MODTRAN-generated SBAFs with those based on observed *Earth Observing-1* (*EO-1*) Hyperion hyperspectral TOA radiances under similar atmospheric conditions. They found that the MODTRAN SBAF-corrected radiance values were too low by 0.5% and 1.5% for Ch1 and Ch2, respectively, compared to those from Hyperion-based SBAFs. Adding the calibration reference and the SBAF difference accounts for the approximately −5% difference between Li and MITRAM. The Li and PATMOS-X calibration differences, available from Li et al. (2015, Table 8), indicate that the latter calibrations in the satellite series differ from those of this study, and are perhaps explained by the fact that Li extrapolated the PATMOS-X coefficients beyond 2009 (C. Li 2015, personal communication). For the morning satellites (*N6*, *N10*, *N12*, and *N15*), the Li calibration is more similar to MITRAM than for NOAA afternoon orbits and thus may indicate calibration differences between the Li Dome-C and desert BRDFs. Because of the noon local equator crossing time (LECT) of the SeaWiFS orbit, the SZA was limited to less than 60° over desert targets and thus near-terminator orbits are based on only Dome-C observations.

b. *Calibration trend differences*

Figures 8c and 8d present the trend differences of the RRMSE of the monthly gains computed from the quadratic calibration coefficients between the three studies and MITRAM after removing the RCB. The three study RRMSEs are mostly near 1.5% and 2% for Ch1 and Ch2, respectively, with respect to MITRAM. The RRMSEs are greater for Ch2 because of differences among the approaches to water vapor absorption pathlength determination and to the SBAF values used by each study. The STAR RRMSEs for *N16* and *N18* are greater than for other sensors because of the relative gain increase as the orbit drifts into near-terminator conditions compared with MITRAM (Fig. 7). The other AVHRR/3 NOAA satellite orbits did not reside as long in terminator conditions. The TIROS-N and *N6* records are very short, and thus their RRMSEs may not be distinguishable from the observation noise. The STAR calibration for the *N14* AVHRR (Nagaraja Rao and Chen 1999) was derived during the first three years of operation, during the more stable part of the record, and applied over the 7-yr record, which did not accurately describe the latter part of the record when the sensor calibration was changing. Given a sufficient temporal record, the three studies have fairly consistent temporal trends, especially for Ch1.

5. Dual-gain counts in GAC Format

Caution must be exercised when comparing AVHRR/3 dual-gain GAC retrievals with other well-calibrated visible sensors. The AVHRR/3 onboard processer averages 4 pixel counts out of every 15 pixels in order to produce the GAC product, corresponding to a nominal 1 km × 4 km pixel resolution. Every third scan line is sampled in the along-track direction, and four out of five contiguous pixel counts are averaged in the scan direction. For AVHRR single-gain instruments, the averaging of single-gain counts maintains the linear response of the sensor. However, for dual-gain instruments, the pixel-level counts are linearly averaged without consideration of either low- or high-gain count status. Initial *Terra* MODIS and *N16* AVHRR SNO radiance pair matching techniques utilized only high-resolution picture transmission (HRPT) or local area coverage (LAC) 1-km nominal pixel resolution full coverage datasets, with simple spatial matching of the 1-km pixels from both satellites (Cao and Heidinger 2002; Heidinger et al. 2002). Considerable matching noise was observed in the initial 1-km-pixel MODIS and AVHRR SNO radiance pair studies. The SNO radiance pair matching noise can be easily mitigated by spatially averaging the AVHRR and MODIS pixel values into larger fields of view (FOV). Wielicki et al. (2008) noted that the *N17*/*N18* AVHRR SNO radiance pair 1σ matching noise was reduced from 5% to 2% by using a 50-km FOV rather than a 12.5-km FOV. Using large FOVs diminishes the navigation errors and time mismatch advection differences.

a. *GAC subsampling compared with LAC*

Large FOVs can also reduce the noise due to GAC subsampling. To illustrate this effect, a LAC Ch1 image encompassing a part of South America and the adjacent Pacific Ocean was selected because of its complex meteorology, containing many cloud and surface types, having significant pixel-to-pixel visible radiance variability. Figure 9a compares the 15-km FOV fully sampled LAC (fifteen 1-pixel mean) counts, which are first converted to single-gain counts and then averaged, with the corresponding subsampled 4-km (four 1-pixel mean) GAC counts, which are first converted to single-gain counts and then averaged (GAC_{single}). Because the 15-km FOV LAC and GAC_{single} counts are from the same image, no navigation or temporal matching noise is introduced. Figure 9d shows the 50-km FOV GAC_{single} and LAC count pairs averaged using a 0.5° latitude × 0.5° longitude grid. Table 6 contains the relevant statistics for Fig. 9. Two linear regressions are computed, one with an unconstrained slope and offset and another with

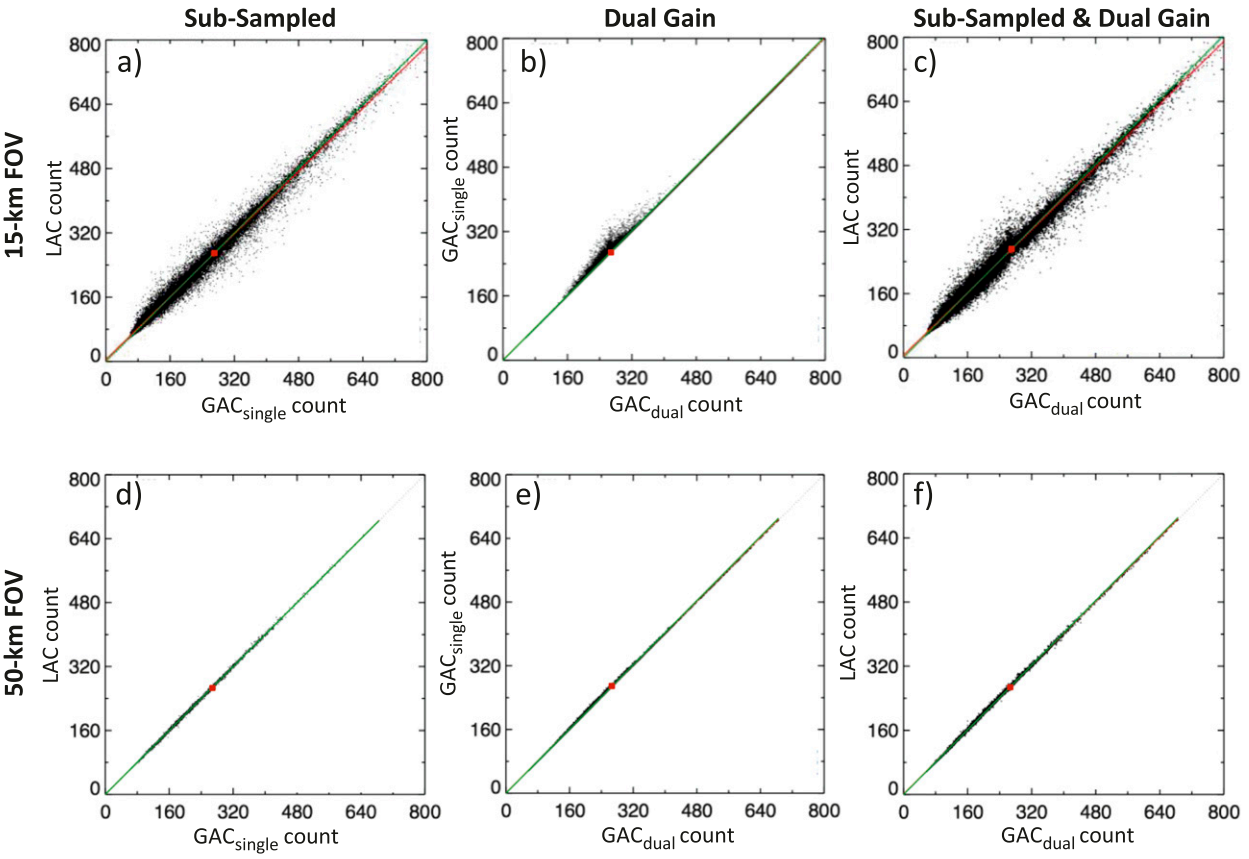

FIG. 9. Scatterplots and linear regression fits based on various combinations of pixel counts from an *N18* AVHRR LAC Ch1 image taken at 1824–1836 UTC 28 Apr 2008. Linear regression was performed using a determinable offset (red line) and a fixed offset (force fit, green line) equal to the space count. The count format is single gain. (a) The mean 15-km FOV LAC count and the corresponding mean GAC_{single} count. (d) As in (a), but for a 50-km FOV. (b) The mean 15-km FOV GAC_{single} count and the mean GAC_{dual} count. (e) As in (b), but for a 50-km FOV. (c) The mean 15-km FOV LAC count and the mean GAC_{dual} count. (f) As in (c), but for a 50-km FOV. The red square denotes the breakpoint count of 275 in single-gain format, which separates the low- and high-gain counts.

the predetermined space count as the offset. This latter regression is referred to as the force fit. The linear regression slopes are 0.9762 and 1.0005 for the 15- and 50-km FOVs, respectively. The 50-km FOV has mitigated the impact of the GAC_{single} subsampling noise. The force fit slopes are 0.9996 and 0.9999 for the 15- and 50-km FOV, respectively; thus, the force fit is closer to the true, unity, slope for both FOVs. As predicted, the standard error of the regression is reduced for larger FOVs. For the AVHRR instruments having a linear (single gain) sensor response, the LAC and GAC_{single} differences should be similar to those of Fig. 9a. Regression using a predetermined offset or large FOV mitigates the impact of GAC subsampling noise.

b. *GAC dual-gain compared with GAC single-gain counts*

Unfortunately, because of the lack of HRPT data and the difficulty of scheduling LAC retrievals over the SNO and invariant target domains, GAC data are often the only recourse for calibration purposes. The onboard GAC processing uses simple linear averages of the pixel counts. To investigate the impact of GAC averaging on dual-gain sensor retrievals, the GAC dual-gain set of four 1-km pixel counts are first averaged and then converted to a single-gain count (GAC_{dual}). This GAC_{dual} count is then compared with the corresponding GAC_{single} count. As expected, dark and bright GAC_{dual} and GAC_{single} count pairs far from the breakpoint are equal (Fig. 9b). However, Fig. 9b clearly shows that the GAC_{dual} count is either less than or equal to the corresponding GAC_{single} count regardless of the low-gain/high-gain breakpoint value of 275 (in terms of single-gain count). In fact, 16% of the GAC_{dual} counts have lower count values than their GAC_{single} count counterparts. The lower GAC_{dual} count is in agreement with Fig. 3 from Doelling et al. (2007), which highlights the regression of GAC dual-gain count and *Meteosat-8*

TABLE 6. Fitting parameters resulting from regression of various combinations of pixel counts from *N18* AVHRR LAC Ch1 image taken at 1824–1836 UTC 28 Apr 2008, plotted in Fig. 9. Linear regression was performed using a determinable offset and a fixed offset (force fit) equal to the space count. The count format is single gain. The subsampled dataset comprises 15-km and 50-km FOV LAC count averages matched with GAC_{single} count averages. The dual-gain dataset is the GAC_{single} counts matched with the corresponding GAC_{dual} counts. The subsampled and dual-gain datasets consist of LAC counts and corresponding GAC_{dual} counts. The last row contains the statistics of the 50-km FOV regression constrained with a 10% spatial homogeneity threshold. The offset units are in 10-bit single-gain counts.

		Linear regression			Force fit	
Dataset	FOV	Slope	Offset	StdErr (%)	Slope	StdErr (%)
Subsampled	15 km	0.9762	5.07	6.89	0.9996	7.04
	50 km	1.0005	−0.12	1.01	0.9999	1.01
Dual gain	15 km	1.0037	0.67	2.53	1.0068	2.63
	50 km	1.0038	0.77	0.85	1.0074	1.14
Subsampled	15 km	0.9803	5.62	7.07	1.0064	7.20
Dual gain	50 km	1.0028	0.98	1.31	1.0075	1.51
	50 km, $<\sigma 10\%$	1.0002	0.14	0.71	1.0008	0.71

radiance pairs. The GAC_{dual} count clearly introduces an artificial increase in the force fit slope of ~0.7% (Table 6). The regression statistics are comparable even for 50-km FOVs. Of the 50-km FOV GAC_{dual} counts, 78% have a lower count value than the associated GAC_{single} counts, although the regression noise is greatly reduced (Fig. 9e). The AVHRR/3 GAC_{dual} count is always less than or equal to the corresponding GAC_{single} or LAC-based count.

c. *GAC subsampling and* ***from dual-gain counts*** *compared with LAC*

To analyze the effects of both GAC subsampling and GAC_{dual} averaging, the GAC_{dual} counts of Fig. 9b and the LAC counts of Fig. 9a are paired and shown in Fig. 9c. Similarly for Fig. 9f, the Fig. 9e GAC_{dual} counts are paired with the LAC counts in Fig. 9d. The force fit slope value is not affected by subsampling, only by whether GAC_{dual} or GAC_{single} counts are used. For the linear regression, the slope and offset are slightly more positive than for the subsampled-only case. To reduce the impact of the GAC_{dual} averaging, a spatial homogeneity filter can be applied. A 10% homogeneity filter, determined by dividing the standard deviation of the individual GAC counts within the FOV by the FOV mean, was applied to the 50-km FOV. The homogeneity filter reduced the 50-km FOV regression standard errors by ~50%. More importantly, the 10% homogeneity filter reduced the force fit slope from 0.75% (1.0075) to 0.08%. Because the DCC and PICS use homogeneity thresholds of 3% and between 5 and 20 counts, respectively, the negative impact of using GAC data should be greatly reduced. Additionally, the DCC and desert invariant target counts do not contain any low-gain counts for most of the sensor record. A homogeneity filter reduces the bias introduced by the AVHRR/3 onboard GAC pixel count averaging process.

d. *Polar SNO domain*

It is uncertain how the GAC_{dual} counts impact the 50-km FOV coincident MODIS and AVHRR SNO radiance pairs located near 80°N. During April through August, there is sufficient sunlight to compute the AVHRR calibration gains. *N18* LAC Ch1 images taken at 1630 UTC 22 April 2008, 1620 UTC 13 June 2008, and 1630 UTC 28 August 2008 were selected to represent SNO conditions during the start, middle, and end of the calibration season. The selected domains encompass Greenland and the Canadian Arctic islands, where both bright snow surfaces and dark clear-sky waters exist. This study uses MODIS radiance and AVHRR SNO 50-km FOV count pairs with a 40% spatial homogeneity threshold applied. The 40% threshold was selected to ensure sufficient sampling over the dynamic range. Therefore, comparisons were performed under these same FOV and filter conditions but using only the portion of the image northward of 70°N, having viewing angles within 20° of nadir, thereby best representing SNO conditions. As expected, the GAC_{dual} count increases the force fit slope from unity for all three LAC image times (Table 7). When the image count value is close to the breakpoint of 275, as is the case on 22 April, the greatest force fit slope of 1.0026 is observed. During June, the higher counts are owed to lower SZAs, whereas during August the smaller counts are due to less snow coverage than in April. Except for the spring months, when most of the domain is snow covered and observed under oblique sun angles, the GAC_{dual} averaging impact is within 0.2% when compared with LAC.

To conclude, the calibration impact of the GAC from dual-gain count averaging has been largely mitigated by

TABLE 7. As in Table 6, but for three images taken over the Arctic, listed by date, and results only for the 50-km FOV LAC count and corresponding *GAC-from-dualgain-count*, with a 40% spatial homogeneity threshold applied. The SNO domain mean count is also given. The mean count and offset units are in 10-bit single-gain counts.

Dataset			Linear regression			Force fit	
Date	UTC	Mean count	Slope	Offset	StdErr (%)	Slope	StdErr (%)
22 Apr	1638	298	0.9966	1.78	0.26	1.0026	0.37
13 Jun	1610	413	0.9952	2.26	0.23	1.0014	0.29
28 Aug	1634	179	1.0033	−0.43	0.14	1.0009	0.20

the MITRAM approach by selecting only homogeneous spatial conditions when calibrating against invariant targets and MODIS. Also, regressions using a large FOV or a predetermined space count minimizes the noise from GAC subsampling. When averaging low- and high-gain counts, the GAC_{dual} averaging always decreases the count when compared to single-gain count averaging. Therefore, when comparing the GAC_{dual}-based cloud and radiation retrievals with other satellite instrument or single-gain AVHRR records, a −0.7% residual radiance bias may exist, especially over the tropics, when using the MITRAM coefficients.

6. Conclusions

The MITRAM calibration, a consistent cross-sensor calibration approach based on multiple desert, polar ice, and DCC invariant targets, was applied to AVHRR solar channel data, producing calibration coefficients for 16 different instruments along with sensor and band specific uncertainties. The calibration approaches were outlined in Part I. Overall, the Ch1 and Ch2 calibration uncertainties for a given sensor are 2% and 3%, respectively (section 2a). Uncertainties for the afternoon satellite AVHRRs are less than those for the morning satellites. Combining the multiple invariant target calibration gains, weighted by the inverse of their temporal variance, produces MITRAM calibration gains with a lower temporal variability than that monitored over any single PICS. PICS with large temporal variances did not adversely impact the MITRAM calibration, which implies that anomalous PICS reflectance drifts are mitigated with this approach. The MITRAM calibration coefficients provide intersensor ρ_{norm} consistencies around 1% and 2% for Ch1 and Ch2, respectively, over the Libya-1, Libya-4, Dome-C, and DCC (section 3). Consistent calibration among various PICS validates both the specific PICS DMs and the SBAFs, which need to be accurate over the large range of SZAs encountered as the NOAA satellite orbits degraded.

All of the invariant targets were referenced to the *Aqua* MODIS calibration using *Aqua* MODIS and *N16* SNOs. The MITRAM and SNO relative calibration biases mostly agreed to within 1% for Ch1 and Ch2 during the *Aqua* MODIS operational period (section 2c). However, the MITRAM calibration does not require contemporary MODIS radiances and can monitor the sensor stability throughout the year, whereas SNO visible observations are available only during the MODIS era for half of any year. Having a common calibration reference allowed the invariant target relative calibration biases with respect to MITRAM to be mostly within 1% and 2% for Ch1 and Ch2, respectively, with corresponding trend RRMSEs of 0.75% and 1.75%, respectively (section 2c). The smaller trend differences suggest that it is easier to determine the relative sensor degradation rather than the magnitude of the calibration gain. Similarly, by comparing MITRAM with three other published AVHHR calibration studies, the relative calibration biases were greater between methods than the trend differences. The relative calibration bias between the different approaches was mostly attributed to the calibration reference source.

Caution must be used when interpreting AVHRR-based retrievals between the AVHRR/3 GAC from the dual-gain count period with respect to the single-gain count period. The GAC_{dual} radiance is ~0.7% less when compared with the LAC or GAC_{single} radiance (section 5). The MITRAM calibration approach mitigates the impact of the GAC_{dual} averaging by using spatial homogeneity thresholds.

The difficulty in calibrating AVHRR sensors owed to the degrading NOAA orbits has long been known (Price 1991). Changes were made to the initial orbit mechanics to lengthen the time to degradation to a terminator orbit. If the NOAA orbits were maintained, as are the MetOp orbits, then only the temporal stability of the invariant target TOA reflectances would determine the accuracy of the calibration because the observed solar and viewing angular geometry would repeat annually. The final AVHRR copy will be launched into a 0930 LECT orbit on MetOp-C in 2018. The last afternoon satellite, *N19*, carrying an AVHRR is more than five years old at the present time. To extend the AVHRR record into the future, the AVHRR, MODIS, and Visible Infrared Imaging Radiometer Suite 1330 LECT sun-synchronous records will need to be combined

as a climate record. Eventually, the AVHRR calibration record can then be tied to a traceable on-orbit calibration sensor, such as the Climate Absolute Radiance and Refractivity Observatory (CLARREO) (Wielicki et al. 2013). Therefore, it is recommended that the AVHRR calibration be referenced to either MODIS or VIIRS, and that improvements be made in the AVHRR calibration algorithms.

Future validation plans include performing AVHRR AM/PM SNO intercalibrations to validate the MITRAM calibration between AM and PM satellite sensors. Sensor- and band-specific polynomial fits of varying order should more accurately describe the calibration drift not captured in a simple second-order fit. The DCC calibration can be improved by increasing the BRDF accuracy for SZA $>$ 40° and by using band-specific DCC BRDFs. *Polarization and Anisotropy of Reflectances for Atmospheric Science Coupled with Observations from a Lidar* (*PARASOL*) observations have shown band-specific DCC BRDF models and thus may prove useful in continued studies (Fougnie et al. 2014). Last, the monitoring of the cross-sensor global mean cloud optical depth retrievals allows all Earth-observed reflected radiances to be evaluated as a whole.

Acknowledgments. The AVHRR satellite data were obtained from NOAA CLASS. The authors thank Karl-Göran Karlsson for independently comparing the MITRAM and PATMOS-X calibration coefficients. Thanks to A. Heidinger for the helpful discussions. This research is supported by the NOAA Climate Data Record Program under Interagency Agreement NOAA-NCDC-CDR-0002. The AVHRR calibration coefficients from this study are contained in the NOAA Climate Data Record (CDR) of Visible and Near Infrared Reflectance from GOES and AVHRR, Version 1.0 (https://www.ngdc.noaa.gov/metaview/page?xml=NOAA/NESDIS/NCDC/Geoportal/iso/xml/C00860.xml&view=getDataView&header=none#Documentation). An algorithm theoretical basis document (ATBD) is also available (Doelling and Minnis 2016).

REFERENCES

Bhatt, R., D. R. Doelling, B. R. Scarino, A. Gopalan, C. O. Haney, P. Minnis, and K. Bedka, 2016: A consistent AVHRR visible calibration record based on multiple methods applicable for the NOAA degrading orbits. Part I: Methodology. *J. Atmos. Oceanic Technol.*, **33**, 2499–2515, doi:10.1175/JTECH-D-16-0044.1.

Cao, C., and A. Heidinger, 2002: Inter-comparison of the longwave infrared channels of MODIS and AVHRR/NOAA-16 using simultaneous nadir observations at orbit intersections. *Earth Observing Systems VII*, W. L. Barnes, Ed., International Society for Optical Engineering (SPIE Proceedings, Vol. 4814), 306, doi:10.1117/12.451690.

——, X. Xiong, A. Wu, and X. Wu, 2008: Assessing the consistency of AVHRR and MODIS L1B reflectance for generating Fundamental Climate Data Records. *J. Geophys. Res.*, **113**, D09114, doi:10.1029/2007JD009363.

Che, N., and J. C. Price, 1992: Survey of radiometric calibration results and methods for visible and near infrared channels of NOAA-7, -9 and -11 AVHRRs. *Remote Sens. Environ.*, **41**, 19–27, doi:10.1016/0034-4257(92)90057-Q.

Cosnefroy, H., M. Leroy, and X. Briottet, 1996: Selection and characterization of Saharan and Arabian desert sites for the calibration of optical satellite sensors. *Remote Sens. Environ.*, **58**, 101–114, doi:10.1016/0034-4257(95)00211-1.

Doelling, D. R., and P. Minnis, 2016: Calibration of historical and future AVHRR and GOES visible and near-infrared sensors. Algorithm Theoretical Basis Doc. CDRP-ATBD-0823, 50 pp. [Available online at https://www.ncdc.noaa.gov/sites/default/files/cdr-documentation/%3Cem%3EEdit%20Climate%20Data%20Record%3C/em%3E%20AVHRR%20Radiances%20-%20NASA/CDRP-ATBD-0823%20AVHRR%20Radiances%20-%20NASA%20C-ATBD%20(01B-30a)%20(DSR-1048).pdf.]

——, D. P. Garber, L. A. Avey, L. Nguyen, and P. Minnis, 2007: The calibration of AVHRR visible dual gain using Meteosat-8 for NOAA-16 to 18. *Atmospheric and Environmental Remote Sensing Data Processing and Utilization III: Readiness for GEOSS*, M. D. Goldberg et al., Eds., International Society for Optical Engineering (SPIE Proceedings, Vol. 6684), 668409, doi:10.1117/12.736080.

——, C. Lukashin, P. Minnis, B. Scarino, and D. Morstad, 2012: Spectral reflectance corrections for satellite intercalibrations using SCIAMACHY data. *Geosci. Remote Sens. Lett.*, **9**, 119–123, doi:10.1109/LGRS.2011.2161751.

——, D. Morstad, B. R. Scarino, R. Bhatt, and A. Gopalan, 2013: The characterization of deep convective clouds as an invariant calibration target and as a visible calibration technique. *IEEE Trans. Geosci. Remote Sens.*, **51**, 1147–1159, doi:10.1109/TGRS.2012.2225066.

——, A. Wu, X. Xiong, B. R. Scarino, R. Bhatt, C. O. Haney, D. Morstad, and A. Gopalan, 2015: The radiometric stability and scaling of Collection 6 Terra and Aqua-MODIS VIS, NIR, and SWIR spectral bands. *IEEE Trans. Geosci. Remote Sens.*, **53**, 4520–4535, doi:10.1109/TGRS.2015.2400928.

Eplee, R. E., Jr., J. Sun, G. Meister, F. S. Patt, X. Xiong, and C. R. McClain, 2011: Cross calibration of SeaWiFS and MODIS using on-orbit observations of the Moon. *Appl. Opt.*, **50**, 120–133, doi:10.1364/AO.50.000120.

Fougnie, B., D. R. Doelling, A. Crespin, B. Lafrance, and L. Labonnote, 2014: Bidirectional reflectance distribution function (BRDF) of deep convective clouds (DCC) derived from PARASOL measurements and compared to radiative transfer computation and model. *2014 CALCON Tech. Conf.*, Logan, UT, Utah State University. [Available online at http://digitalcommons.usu.edu/calcon/CALCON2014/All2014Content/7/.]

Heidinger, A. K., C. Cao, and J. T. Sullivan, 2002: Using Moderate Resolution Imaging Spectrometer (MODIS) to calibrate advanced very high resolution radiometer reflectance channels. *J. Geophys. Res.*, **107**, 4702, doi:10.1029/2001JD002035.

——, W. C. Straka III, C. C. Molling, and J. T. Sullivan, 2010: Deriving an inter-sensor consistent calibration for the AVHRR solar reflectance data record. *Int. J. Remote Sens.*, **31**, 6493–6517, doi:10.1080/01431161.2010.496472.

Li, C., Y. Xue, Q. Liu, J. Guang, X. He, J. Zhang, T. Wang, and X. Liu, 2014: Post calibration of channels 1 and 2 of long-term

AVHRR data record based on SeaWiFS data and pseudo-invariant targets. *Remote Sens. Environ.*, **150**, 104–119, doi:10.1016/j.rse.2014.04.020.

——, ——, ——, K. Ouzzane, and J. Zhang, 2015: Using SeaWiFS measurements to evaluate radiometric stability of pseudo-invariant calibration sites at top of atmosphere. *IEEE Geosci. Remote Sens. Lett.*, **12**, 125–129, doi:10.1109/LGRS.2014.2329138.

Lyapustin, A., and Coauthors, 2007: Analysis of MODIS–MISR calibration differences using surface albedo around AERONET sites and cloud reflectance. *Remote Sens. Environ.*, **107**, 12–21, doi:10.1016/j.rse.2006.09.028.

Mittaz, J., and A. Harris, 2011: A physical method for the calibration of the AVHRR/3 thermal IR channels. Part II: An in-orbit comparison of the AVHRR longwave thermal IR channels on board *MetOp-A* with IASI. *J. Atmos. Oceanic Technol.*, **28**, 1072–1087, doi:10.1175/2011JTECHA1517.1.

Molling, C. C., A. K. Heidinger, W. C. Straka, and X. Wu, 2010: Calibrations for AVHRR channels 1 and 2: Review and path towards consensus. *Int. J. Remote Sens.*, **31**, 6519–6540, doi:10.1080/01431161.2010.496473.

Nagaraja Rao, C. R., and J. Chen, 1995: Inter-satellite calibration linkages for the visible and near-infrared channels of the Advanced Very High Resolution Radiometer on the NOAA-7, -9, and -11 spacecraft. *Int. J. Remote Sens.*, **16**, 1931–1942, doi:10.1080/01431169508954530.

——, and ——, 1999: Revised post-launch calibration of the visible and near-infrared channels of the Advanced Very High Resolution Radiometer (AVHRR) on the NOAA-14 spacecraft. *Int. J. Remote Sens.*, **20**, 3485–3491, doi:10.1080/014311699211147.

——, M. P. Weinreb, and J. Chen, 1994: Recalibration of the Advanced Very High Resolution Radiometer for climate change research. *Adv. Space Res.*, **14A**, 117–120, doi:10.1016/0273-1177(94)90359-X.

Price, J. C., 1991: Timing of NOAA afternoon passes. *Int. J. Remote Sens.*, **12**, 193–198, doi:10.1080/01431169108929644.

Rossow, W. B., and J. Ferrier, 2015: Evaluation of long-term calibrations of the AVHRR visible radiances. *J. Atmos. Oceanic Technol.*, **32**, 744–766, doi:10.1175/JTECH-D-14-00134.1.

Scarino, B., D. R. Doelling, P. Minnis, A. Gopalan, T. Chee, R. Bhatt, C. Lukashin, and C. O. Haney, 2016: A web-based tool for calculating spectral band difference adjustment factors derived from SCIAMACHY hyper-spectral data. *IEEE Trans. Geosci. Remote Sens.*, **54**, 2529–2542, doi:10.1109/TGRS.2015.2502904.

Smith, G. R., R. H. Levin, P. Abel, and H. Jacobowitz, 1998: Calibration of the solar channels of the NOAA-9 AVHRR using high altitude aircraft measurements. *J. Atmos. Oceanic Technol.*, **19**, 1826–1833, doi:10.1175/1520-0426(1988)005<0631:COTSCO>2.0.CO;2.

Sun, J., A. Angal, X. Xiong, H. Chen, X. Geng, A. Wu, T. Choi, and M. Chu, 2012: MODIS reflective solar bands calibration improvements in Collection 6. *Earth Observing Missions and Sensors: Development, Implementation, and Characterization II*, H. Shimoda et al., Eds., International Society for Optical Engineering (SPIE Proceedings, Vol. 8528), 85280N, doi:10.1117/12.979733.

——, X. Xiong, A. Angal, H. Chen, A. Wu, and X. Geng, 2014: Time-dependent response versus scan angle for MODIS reflective solar bands. *IEEE Trans. Geosci. Remote Sens.*, **52**, 3159–3174, doi:10.1109/TGRS.2013.2271448.

Weatherhead, E. C., and Coauthors, 1998: Factors affecting the detection of trends: Statistical considerations and applications to environmental data. *J. Geophys. Res.*, **103**, 17 149–17 161, doi:10.1029/98JD00995.

Wielicki, B. A., D. R. Doelling, D. F. Young, N. G. Loeb, D. P. Garber, and D. G. MacDonnel, 2008: Climate quality broadband and narrowband solar reflected radiance calibration between sensors in orbit. *2008 IEEE International Geoscience and Remote Sensing Symposium*, Vol. 1, IEEE, I-257–I-260, doi:10.1109/IGARSS.2008.4778842.

——, and Coauthors, 2013: Achieving climate change absolute accuracy in orbit. *Bull. Amer. Meteor. Soc.*, **94**, 1519–1539, doi:10.1175/BAMS-D-12-00149.1.

Wu, A., X. Xiong, and A. Angal, 2013a: Deriving a MODIS-based calibration for the AVHRR reflective solar channels of the NOAA KLM operational satellites. *IEEE Trans. Geosci. Remote Sens.*, **51**, 1405–1413, doi:10.1109/TGRS.2012.2220780.

Wu, X., J. T. Sullivan, and A. K. Heidinger, 2010: Operational calibration of the Advanced Very High Resolution Radiometer (AVHRR) visible and near-infrared channels. *Can. J. Remote Sens.*, **36**, 602–616, doi:10.5589/m10-080.

Xiong, X., W. Barnes, K. Chiang, H. Erives, N. Che, and J. Sun, 2004: Status of Aqua MODIS on-orbit calibration and characterization. *Sensors, Systems, and Next-Generation Satellites VIII*, R. Meynart, S. P. Neeck, and H. Shimoda, Eds., International Society for Optical Engineering (SPIE Proceedings, Vol. 5570), 317–327, doi:10.1117/12.564940.

——, J. Sun, A. Wu, K -F. Chiang, J. Esposito, and W. Barnes, 2005: Terra and Aqua MODIS calibration algorithms and uncertainty analysis. *Sensors, Systems, and Next-Generation Satellites IX*, R. Meynart, S. P. Neeck, and H. Shimoda, Eds., International Society for Optical Engineering (SPIE Proceedings, Vol. 5978), 59780V, doi:10.1117/12.627631.

Yu, F., and X. Wu, 2010: Water vapor correction to improve the operational calibration for NOAA AVHRR/3 channel 2 (0.85 μm) over a desert target. *Can. J. Remote Sens.*, **36**, 514–526, doi:10.5589/m10-077.

——, ——, M. Grotenhuis, and H. Qian, 2014: Intercalibration of GOES Imager visible channels over the Sonoran Desert. *J. Geophys. Res. Atmos.*, **119**, 8639–8658, doi:10.1002/2013JD020702.